Numerical and analytical investigation of the indirect noise in a nozzle

M. Leyko*[,a], S. Moreau[b], F. Nicoud[c], T. Poinsot[d]

[a] *SNECMA, Villaroche, France - CERFACS, Toulouse, France*
[b] *GAUS, Faculté de Génie, Université de Sherbrooke, Canada*
[c] *I3M, Université Montpellier II, UMR CNRS 5149, France*
[d] *Institut de Mécanique des Fluides, Université de Toulouse, CNRS, France*

Abstract

Analytical and numerical assessments of the indirect noise generated through a nozzle are presented. The configuration corresponds to an experiment achieved at DLR by Bake *et al.* [F. Bake, C. Richter, B. Mühlbauer, N. Kings, I. Röhle, F. Thiele, B. Noll, The entropy wave generator (ewg): a reference case on entropy noise, Journal of Sound and Vibration 326 (2009) 574-598] where an entropy wave is generated upstream of a nozzle by an electrical heating device. Both 3-D and 2-D axisymmetric simulations are performed to demonstrate that the experiment is mostly driven by linear acoustic phenomena, including pressure wave reflection at the outlet and entropy-to-acoustic conversion in the accelerated regions. Moreover, the spatial inhomogeneity of the upstream entropy fluctuation has no visible effect for the investigated frequency range (0-100 Hz). Similar results are obtained with a purely analytical method based on the compact nozzle approximation of Marble and Candel [F. Marble, S. Candel, Acoustic disturbances from gas nonuniformities convected through a nozzle, Journal of Sound and Vibration 55 (1977) 225-243] demonstrating that the DLR results can be reproduced simply on the basis of a low-frequency compact-elements approximation. Like in simulations, the analytical method shows that the acoustic

*Corresponding author.
Email addresses: leyko@cerfacs.fr (M. Leyko), stephane.moreau@usherbrooke.ca (S. Moreau), franck.nicoud@univ-montp2.fr (F. Nicoud), thierry.poinsot@imft.fr (T. Poinsot)

impedance downstream of the nozzle must be accounted for to properly recover the experimental pressure signal. The analytical method can also be used to optimize the experimental parameters and avoid the interaction between transmitted and reflected waves.
Key words: aeroacoustics, indirect combustion noise, nozzle flow
PACS:

Nomenclature

$\mathcal{A}$	Nozzle cross-section area
c_p	Fluid heat capacity at constant pressure
c_v	Fluid heat capacity at constant volume
c	Speed of sound
d	Empirical smoothing constant
L^-	Entering wave at outlet boundary
ℓ_{in}	Length of the inlet duct upstream of the nozzle throat
ℓ_{out}	Length of the exit domain downstream of the nozzle throat
ℓ_h	Length of the experimental heating zone
$\mathcal{M} = u/c$	Fluid Mach number
$\dot{m}$	Fluid mass flow rate
p	Fluid static pressure
p_{ref}	Reference static pressure
p_B	Outlet nodal static pressure
P^-	Acoustic pressure propagating downstream
P^+	Acoustic pressure propagating upstream
r	Radial distance to the axis
R	Upstream duct radius
$\mathcal{R}_{\text{in}}, \mathcal{R}_{\text{out}}$	Acoustic reflection coefficient at the simulation inlet and exit
$\mathcal{R}_1, \mathcal{R}_4$	Acoustic reflection coefficient in planes 1 and 4
s	Fluid entropy
t	Time

t_0	Time of electrical device trigger
T	Fluid static temperature
T_p	Pulse duration
T_t	Fluid total or stagnation temperature
u	Fluid velocity
x	Axial coordinate of the nozzle
x_0	Average location of the source term and position of the heating device
γ	Fluid heat capacity ratio
Δt	Time step
κ	Relaxation coefficient on pressure at the outlet boundary
ρ	Fluid density
σ	Reduced entropy fluctuation
τ	Relaxation time of the pulse model
ϕ	Temporal variation of the electrical device source term
Φ	Source term in the energy equation
Φ_0	Amplitude of the source term in the energy equation
ω	Angular frequency

1. Introduction

Over the last five decades, jet and external aerodynamic noises of aircraft have been substantially reduced. Further developments will be needed for modern aircraft design in order to meet the increasingly restrictive rules about noise reduction; there is no doubt that Computational AeroAcoustics (CAA) will play a major role in these future developments. With the drastic reduction of jet noise already achieved, the relative importance of other noise sources has increased and the contribution of these sources must be controlled if further global noise reduction is to be achieved. Among these sources, the noise coming from the turbulent flame within the combustor is already identified as significant at

take-off, especially in the mid-frequency range.

Two main mechanisms controlling noise propagation from the combustion chamber to the far field have been identified (1; 2; 3)(see Fig. 1). On the one hand, acoustic perturbations generated by the unsteady heat release from the turbulent flame (4) propagate either upstream or downstream through the turbomachinery stages and can reach the far field after being distorted by the mean flow as well as diffracted and reflected by the solid walls within the diffuser, the distributer and the turbine and compressor blades. This sound generation is the *direct combustion noise*. On the other hand, entropy fluctuations generated within the combustion chambers (hot spots, imperfect mixing, etc.) are propagated downstream and interact with the accelerating mean flow. During this interaction, part of the energy contained in the entropy modes is transferred into the acoustic modes and the subsequent acoustic waves are transmitted to the far field through the turbine stages in a similar way as for the direct combustion noise. This mechanism is called the *indirect combustion noise* and is the main focus of the present study.

In the seventies, a significant experimental and modeling effort of engine core noise was undertaken (5; 6; 7; 3; 8). In these experiments, however, the amplitude of the induced temperature fluctuation (about 1 K) was too low to clearly measure and characterize the indirect noise. An analytical model for the indirect combustion noise for compact nozzles was proposed by Marble and Candel (9). Moase *et al.* (10) have recently extended the analytical results of Marble and Candel (9) for choked nozzles and supersonic nozzles of arbitrary geometry to study the conditions for unchoke, "over-choke" and unstart. By numerically solving the quasi-one-dimensional Euler equations they carefully studied the non-linear and non-compact phenomena to which the above analytical results do not apply. Stow *et al.* (11) also generalized the analytical results of Marble and Candel (9) by removing the quasi-one-dimensional assumption and moving to two-dimensional axisymmetric flow to study the reflection of azimuthal modes in choked nozzles. The resulting Euler equations were linearized and solved numerically. Yet no actual dedicated experimental validation of those

theorical and numerical results with significant entropy waves generated were achieved until the recent entropy wave generator (EWG) experiment at DLR by Bake *et al.* (12; 13; 14; 15; 16). The corresponding experimental setup and the major measurements are summarized in Sec. 2.

From the current knowledge and expertise in Large Eddy Simulations (LES) of turbulent reacting flows in complex geometries and the accuracy requirements of direct noise prediction (CAA), computing the absolute level of combustion noise from a realistic combustor is probably out of reach of the present computing and modelling capabilities and starts from a *model* experiment such as the DLR EWG set-up is a logical first step. In this framework, the objectives of this study are threefold. First, the capability of a state-of-the-art LES code (ABVP) to compute compressible reacting flows and reproduce the entropy/acoustic interaction in the presence of a strong mean velocity gradient is assessed. The associated computational domain and simulations are discussed in Sec. 3.1 where a short description of the LES solver used here is also provided. The numerical results are then compared to the measurements from the EWG experiment and to the recent URANS computations achieved by Mühlbauer *et al.* (17). Secondly, the first-order physical mechanisms that drive the pressure signal measured in the experiment are explored. Notably the effects of (a) the entropy fluctuations shape and size, and (b) the boundary conditions are assessed. Finally, the application range of the analytical approach based on the compact nozzle approximation (9; 18) and valid for plane waves is investigated in Sec. 4. The analytical relationships that can be derived for unchoked and choked nozzles are first reviewed and applied to the EWG configuration and flow conditions. The analytical results are then compared with both the experimental data of Bake *et al.* (16) and the present unsteady simulations.

2. DLR experimental set-up and measurements

All computations presented in this paper are related to the DLR experimental setup studied by Bake *et al.* (13; 14; 15; 16). A sketch of the so-called

Convergent length	Divergent length	Throat diameter	Inlet diameter	Exit diameter
13 mm	250 mm	7.5 mm	30 mm	40 mm

Table 1: Main geometrical characteristics of the DLR experimental nozzle

Entropy Wave Generator (EWG) experiment is displayed in Fig. 2. It consists of a tube fed by entropy waves generated by an electric heating device located between the upstream plenum and the nozzle. The main geometrical parameters of the experiment are summarized in Table 1. The operating conditions were varied from unchoked conditions (nozzle Mach numbers, M_{nozzle}, from 0.15 to 0.9) to choked flows ($M_{nozzle} = 1$) with various exit Mach numbers, M_{exit}. The averaged amplitude of the temperature fluctuations was also varied.

The present numerical simulations are restricted to the conditions termed reference test case 1 by Bake *et al.* (16). The nozzle is choked but not adapted so that a normal shock takes place just after the throat, within the divergent section. When accelerated through the nozzle, the small amplitude entropy fluctuations (in the order of 10 K) produce backward and forward propagating acoustic waves. The forward part of the generated noise is measured by microphones located downstream of the nozzle. The main physical parameters defining the operating conditions are presented in Table 2. It should be stressed that the heating duration is 100 ms which, with a bulk velocity in the order of 12 m/s, leads to an entropy perturbation of typical length in the order of 1200 mm while the nozzle is about 263 mm long. This is most likely not relevant to practical engine applications where the expected length of the entropy spots is of the order of 100-200 mm. Further details of the experiment and the associated measurements can be found in Bake *et al.* (14; 15).

Plenum pressure	Outlet pressure	Inlet Mach
117,000 Pa	100,800 Pa	0.037
Outlet Mach	Pulse duration, τ	Pulse amplitude
0.023	100 ms	9 K

Table 2: Main physical parameters of the DLR Entropy Wave Generator experiment

3. Numerical simulation of indirect noise

3.1. Numerical set-ups and parameters

The numerical tool used in this study is the unstructured combustion code AVBP developed at CERFACS (19; 20). AVBP solves the complete three-dimensional compressible Navier-Stokes equations. It therefore integrates all possible non-linear effects involved in the entropy noise generation and contained in the these equations. The unstructured approach allows meshing and computing not only the nozzle but also the whole air feeding line as well as the exhaust system. This formulation then naturally accounts for the energy transfer between the entropy and the acoustic modes, and for the actual, possibly non-compact, nozzle geometry. The numerical method used in AVBP is based on a weighted residual, Taylor-Galerkin discretization which is third-order in both space and time (21) in order to minimize the dispersion and dissipation errors.

The main characteristics of the simulations are presented in Table 3. The entries "short" and "long" refer to the two types of computational domain depicted in Fig. 2. They both include the upstream plenum and the heating section but the "short" one extends only 500 mm downstream of the nozzle throat (length ℓ_{out}) while the "long" contains the exhaust duct up to the inlet of the anechoic section, viz. approx. 2100 mm downstream of the nozzle. In Table 3, "BC" refers to the boundary condition prescribed at the outlet of the computational domain which can be either non-reflecting, fully reflecting or corresponds to a finite (neither zero nor infinite) acoustic impedance. The "heating" entries correspond to the shape of the temperature pulse: it is 1-D

in most cases (viz. uniform in the plane normal to the duct) expected for case 2D-2 where it depends on the distance r to the axis (viz. non-uniform in the cross-section; in the present case, the heating source term is proportional to $\cos[(r/R)(\pi/2)]$, with R the radius of the upstream duct). The uniform and non-uniform heating cases correspond to the same overall energy so that the comparison between runs 2D-1 and 2D-2 can provide relevant information on the effects of the inhomogeneity of the entropy perturbation. In the same way, comparing runs 2D-1 and 2D-3 will provide information about the sensitivity of the results to the outlet boundary condition while comparing 3D-1 and 2D-1 will be relevant to quantify 3-D effects. Finally, run 2D-4 is designed to mimic, as much as possible, the experimental downstream acoustic impedance which was evaluated by DLR. In all cases, the mesh resolution is enough to represent the propagation of the entropy and acoustic waves in the duct without significant dissipative and dispersive errors. The mesh size is of the order of 1 mm and allows a sufficient resolution of the perturbation size (of the order of 1200 mm, see Sec.2). The 3-D mesh contains 1.2 million tetraedras, corresponding to approximately 15 cells in a cross-section. The mesh density is equivalent for all 2-D axisymmetric cases.

In order to mimic the experimental heating device, a source term is added to the energy equation. It reads:

$$\Phi(x,t) = \Phi_0 \frac{1}{2}\left[\tanh\left(\frac{x - x_0 + \ell_h/2}{d}\right)\tanh\left(-\frac{x - x_0 - \ell_h/2}{d}\right) + 1\right]\phi(t)$$

where $\ell_h = 30$ mm is representative of the length of the experimental heating zone and $d = 3$ mm enables to sufficiently smooth the source term to avoid numerical issues. Moreover, the average location x_0 of the source term has been consistently chosen at the location of the electrical device in the experiment (100 mm upstream of the nozzle throat). The temporal evolution $\phi(t)$ is defined as the following:

$$\phi(t) = \begin{cases} 1 - e^{-\frac{t-t_0}{\tau}} & \text{if } t \in [t_0, t_0 + T_p] \\ \phi(t_0 + T_p)e^{-\frac{t-t_0}{\tau}} & \text{if } t > t_0 + T_p \end{cases}$$

Run	Geometry	Length	BC	Heating
3D-1	3D	short	non-reflecting	uniform
2D-1	2D axi	short	non-reflecting	uniform
2D-2	2D axi	short	non-reflecting	non-uniform
2D-3	2D axi	short	reflecting	uniform
2D-4	2D axi	long	finite impedance	uniform

Table 3: Main characteristics of the small-scale simulations.

where t_0 is the time when the electrical device is triggered, T_p is the pulse duration set to 100 ms and τ is a relaxation time of the pulse set to 8 ms. As shown in Fig. 3, these numerical parameters allow a fair representation of the temperature fluctuation produced in the DLR experiment. This temperature perturbation passes through the nozzle, gets distorted and yields pressure fluctuations which are analysed in the next section.

3.2. Numerical results

The time traces of the pressure computed 350 mm downstream of the throat (solid lines) are displayed in Fig. 4 for runs 2D-1 (top left), 2D-2 (top right), 2D-3 (bottom left) and 3D-1 (bottom right). They are compared to the experimental signal (dashed lines). Clearly enough, these simulations do not reproduce the experimental data, neither in terms of amplitude, nor in terms of signal shape. For runs 2D-1 and 3D-1, the numerical pressure trace has a top-hat behavior similar to the temperature upstream fluctuation, while the experiment shows a wavy behavior at a frequency close to 30 Hz. Figure 4 also indicates that 3D-1 leads to results very similar to 2D-1, indicating that the disagreement between the 2D-1 computation and the experimental data cannot be attributed to three-dimensional effects. The same conclusion can be drawn by comparing 2D-1 and 2D-2 for the temperature inhomogeneity which appears to have no effect, at least for this configuration. On the other hand, Fig. 4 illustrates how large the effects of the downstream acoustic boundary condition can be. When a fully reflecting condition (2D-3),which imposes pressure is used instead of a non-reflecting one

(2D-1), which essentially sets the incoming acoustic wave to zero at the outlet, the amplitude decreases drastically. More importantly, the shape of the signal is also strongly modified by the superposition of the downward and backward pressure waves. A wavy behavior is also obtained in run 2D-3, although with a characteristic amplitude and a frequency in quantitative disagreement with the experiment and the simulations reported by Mühlbauer *et al.* (17; 22) (Fig. 10 in this reference). The amplitude is all the more reduced as the computational exit duct is shortened.

The previous results suggest that the discrepancies observed in Fig. 4 might be related to an incorrect downstream acoustic impedance as already suggested by Mühlbauer *et al.* (17; 22) and Leyko *et al.* (23; 24). Indeed, the short computational domain and non-reflecting BC used in runs 2D-1, 2D-2 and 3D-1 would only be representative of the actual experimental conditions if a perfect anechoic system would have been used by Bake *et al.* (16). It should also be noted that a slight reflectivity of the outlet boundary condition in the simulation distorts the pressure responses that get damped around 0.1 s as in the URANS simulation by Mühlbauer *et al.* (22) (Fig. 11 in this reference), which stresses the high sensitivity of the simulations to the exit flow condition. Actually, Fig. 5 demonstrates that substantial reflection occured in the experiment, especially in the low-frequency range: the modulus of the reflection coefficient, defined as the ratio of the backward wave to forward wave at the outlet, is as large as 0.5 at 30 Hz, the typical frequency of the reflections observed in the experimental signal (see Fig. 4). Accounting for a complex-valued, frequency-dependent reflection coefficient in a CFD code solving the flow equations in the time-domain is not trivial. Reymen *et al.* provide an efficient time-domain impedance boundary condition (25) using Tam and Auriault's method (26). Rienstra also proposed a method to take into account time-domain impedance (27), but all these aproaches are exact only for a given frequency. Broadband impedance models based on z-transform have been investigated by Ozyoruk *et al.*, but are sensitive to instabilities (28). A simpler approach has been followed in the present study. Instead of using a non-reflecting outlet boundary condition with zero entering

wave L^-, it is common use to write the latter as a pressure difference times a relaxation coefficient κ (29), viz. $L^- = 2\kappa\Delta t(p_{\text{ref}} - p_B)/(\rho c)$, with Δt the time step, p_B the nodal pressure at the outlet boundary and p_{ref} the reference pressure. In doing so, the outlet condition acts as a first-order low pass filter (30) whose cut-off frequency is proportional to κ and the acoustic reflection coefficient $\mathcal{R}_{\text{out}}$ reads:

$$\mathcal{R}_{\text{out}} = -\frac{1}{\imath\omega/\kappa + 1} \tag{1}$$

It is thus possible to tune the relaxation coefficient κ in order to reproduce the amplitude of the experimental reflection coefficient, at least in the low-frequency range. The length ℓ_{out} of the downstream duct is then tuned to mimic the experimental time delay as well as to compensate for the phase of the relaxation-based outlet partially reflecting condition. The experimental reflection coefficient is expressed here at the nozzle throat ($x = 0$) while the reflection coefficient of the numerical boundary condition, Eq. (1), is given at the end of the computational domain ($x = \ell_{\text{out}}$). Assuming the Mach number to be small in the outlet duct, the experimental reflection coefficient can be multiplied by $\exp(-2\imath\ell_{\text{out}}\omega/c)$ in order to shift it to the same position, at the end of the numerical domain ($x = \ell_{\text{out}}$). The experimental reflection coefficient obtained in this way is depicted in Fig. 5 where a fair agreement with the numerical one is apparent in the frequency range 20-40 Hz. The best-fit relaxation coefficient κ and length ℓ_{out} are close to 160 s^{-1} and 2100 mm respectively. As soon as this corrected impedance is used at the outlet, results improve drastically: Fig. 6 indicates that the numerical pressure signal is in better agreement with the measured one when accounting for the effective downstream boundary condition, and so for all positions of the pressure sensor downstream of the nozzle.

4. An analytical method for indirect noise computation

An analytical model for the indirect combustion noise was proposed by Marble and Candel (9), which focused on the generation and the transmission of flow perturbations (acoustic and entropy) through a steady non-uniform nozzle flow.

Assuming a quasi-one-dimensional nozzle flow and quasi-steady perturbations (nozzle compactness), they established the relationships linking the different perturbations using first principles only: mass flow, energy and entropy conservations. These developments are reviewed below and extended to the case of a shock in a nozzle to obtain an analytical tool which completely describes the DLR experiment and can replace the numerical simulation. The extended analytical results giving relations between waves in all possible cases (unchoked insentropic nozzle, choked insentropic nozzle and shock in nozzle) are then used to obtain the pressure fluctuations in the EWG experiments. Partially reflective boundary conditions identical to those used in the LES cases are also introduced in the model both at the inlet and outlet of the domain. By comparing with the above simulations with identical acoustic impedances at both inlet and outlet, the domain of validity of the compact nozzle assumption and the linear regime inherent to the analytical approach can be assessed.

4.1. Isentropic nozzle

An isentropic flow of a homogeneous gas of density ρ, velocity u, pressure p, constant heat capacities c_p and $c_v = c_p/\gamma$ is assumed in a quasi-1-D adiabatic duct of cross-section area $\mathcal{A}(x)$ as shown in Fig. 7. In this case, the mass flow rate

$$\dot{m} = \rho u \mathcal{A}, \tag{2}$$

the stagnation temperature

$$T_t = T\left(1 + \frac{\gamma - 1}{2}\mathcal{M}^2\right), \tag{3}$$

and the entropy

$$s = c_v \; log\frac{p}{\rho^\gamma}, \tag{4}$$

are constant throughout the duct. Eqs. (2), (3) and (4) can be differentiated to yield the corresponding fluctuations:

$$\frac{\dot{m}'}{\dot{m}} = \frac{1}{\mathcal{M}}\frac{u'}{c} + \frac{p'}{\gamma p} - \frac{s'}{c_p} \tag{5}$$

$$\frac{T_t'}{T_t} = \frac{1}{1+\frac{\gamma-1}{2}\mathcal{M}^2}\left[(\gamma-1)\mathcal{M}\frac{u'}{c} + (\gamma-1)\frac{p'}{\gamma p} + \frac{s'}{c_p}\right] \tag{6}$$

and

$$\frac{s'}{c_p} = \frac{p'}{\gamma p} - \frac{\rho'}{\rho}, \tag{7}$$

where the speed of sound $c = \sqrt{\gamma p/\rho}$ and the Mach number $\mathcal{M} = u/c$ have been introduced.

If the wavelengths of the perturbations are large compared with the axial dimension of the nozzle (compact nozzle assumption), there is no delay and distortion between the inlet and the outlet sections of the nozzle. As a result, the instantaneous values of the mass flow, the total temperature and the entropy are conserved throughout the nozzle at each instant, as displayed in Fig. 8. In other words, the compact nozzle assumption allows writing the following equations:

$$[T_t']_a^b = 0 \quad ; \quad [\dot{m}']_a^b = 0 \quad ; \quad [s']_a^b = 0 \tag{8}$$

where $[\ ]_a^b$ stands for the jump between downstream (index b) and upstream (index a) of the related object (subcritical nozzle, supercritical nozzle and normal shock). At this point, it is useful to introduce the following acoustic waves and reduced amplitudes (9):

$$P^+ = \frac{1}{2}\left(\frac{p'}{\gamma p} + \frac{u'}{c}\right) \quad ; \quad P^- = \frac{1}{2}\left(\frac{p'}{\gamma p} - \frac{u'}{c}\right) \quad ; \quad \sigma = \frac{s'}{c_p} \tag{9}$$

4.1.1. Unchoked nozzle

By combining Eqs. (8) with Eqs. (5), (6) and (7), the following set of three equations can be obtained:

$$\begin{aligned}
\left(1+\frac{1}{\mathcal{M}_a}\right)P_a^+ + \left(1-\frac{1}{\mathcal{M}_a}\right)P_a^- - \sigma_a &= \\
\left(1+\frac{1}{\mathcal{M}_b}\right)P_b^+ + \left(1-\frac{1}{\mathcal{M}_b}\right)P_b^- - \sigma_b & \\
\frac{(\gamma-1)(1+\mathcal{M}_a)}{1+\frac{\gamma-1}{2}\mathcal{M}_a^2}P_a^+ + \frac{(\gamma-1)(1-\mathcal{M}_a)}{1+\frac{\gamma-1}{2}\mathcal{M}_a^2}P_a^- + \frac{1}{1+\frac{\gamma-1}{2}\mathcal{M}_a^2}\sigma_a &= \\
\frac{(\gamma-1)(1+\mathcal{M}_b)}{1+\frac{\gamma-1}{2}\mathcal{M}_b^2}P_b^+ + \frac{(\gamma-1)(1-\mathcal{M}_b)}{1+\frac{\gamma-1}{2}\mathcal{M}_b^2}P_b^- + \frac{1}{1+\frac{\gamma-1}{2}\mathcal{M}_b^2}\sigma_b & \\
\sigma_a &= \sigma_b
\end{aligned} \tag{10}$$

In each of the previous equations, the left-hand-side involves the three waves (P_a^+, P_a^-, σ_a) upstream of the nozzle at the inlet and the right-hand-side the three waves (P_b^+, P_b^-, σ_b) downstream of the nozzle at the outlet. As shown in Fig. 7, these waves propagate either outward or inward (toward the nozzle) depending on the flow-characteristic directions at these subsonic boundaries. In the particular case where $P_a^+ \neq 0$, $\sigma_a = 0$ and $P_b^- = 0$ (the ingoing waves can be fixed freely), Eqs. (10) allow recovering the expression given in (9) for the acoustic response of the unchoked nozzle to an acoustic excitation (AA):

$$\frac{P_b^+}{P_a^+}(\text{AA}) = \frac{2\mathcal{M}_b}{1+\mathcal{M}_b}\,\frac{1+\mathcal{M}_a}{\mathcal{M}_a+\mathcal{M}_b}\,\frac{1+\frac{1}{2}(\gamma-1)\mathcal{M}_b^2}{1+\frac{1}{2}(\gamma-1)\mathcal{M}_a\mathcal{M}_b} \tag{11}$$

In the same way, if $P_a^+ = 0$, $\sigma_a \neq 0$ and $P_b^- = 0$ are assumed, the acoustic response to an entropy perturbation (SA) is recovered as in (9), viz.:

$$\frac{P_b^+}{\sigma_a}(\text{SA}) = \frac{\mathcal{M}_b-\mathcal{M}_a}{1+\mathcal{M}_b}\,\frac{\frac{1}{2}\mathcal{M}_b}{1+\frac{1}{2}(\gamma-1)\mathcal{M}_a\mathcal{M}_b} \tag{12}$$

4.1.2. Isentropic choked nozzle

In the case of an isentropic choked nozzle, the flow is subsonic in the convergent nozzle part and supersonic in the divergent nozzle part. In this case, the acoustic wave P_b^- leaves the domain and cannot be imposed anymore (Fig. 9). Two waves enter the domain, namely P_a^+ and σ_a, and four must be determined, namely three transmitted/generated waves (P_b^+, P_b^- and σ_b) and one reflected/generated wave (P_a^-). The critical mass flow equation is then introduced in order to close the problem ($\mathcal{A}^\star$ being the critical section area and $\dot{m}^\star$ being the critical mass flow):

$$\dot{m}^\star = \frac{p_{t1}}{\sqrt{\gamma r T_{t1}}}\mathcal{A}^\star\gamma\left(\frac{\gamma+1}{2}\right)^{-\frac{1}{2}\frac{\gamma+1}{\gamma-1}} \tag{13}$$

By first differentiating Eq. (13) and combining the result with Eq. (5), the following additional condition can be obtained for the fluctuations:

$$\frac{u'}{c} - \frac{\gamma-1}{2}\mathcal{M}\frac{p'}{\gamma p} - \frac{1}{2}\mathcal{M}\frac{s'}{c_p} = 0 \tag{14}$$

which can be used to complete Eqs. (8) and close the system. After some algebra the following expressions for the four outgoing waves can be obtained:

$$\begin{aligned}
\left(1-\frac{\gamma-1}{2}\mathcal{M}_a\right)P_a^+ - \left(1+\frac{\gamma-1}{2}\mathcal{M}_a\right)P_a^- - \frac{1}{2}\mathcal{M}_a\sigma_a &= 0 \\
\left(1-\frac{\gamma-1}{2}\mathcal{M}_b\right)P_b^+ - \left(1+\frac{\gamma-1}{2}\mathcal{M}_b\right)P_b^- - \frac{1}{2}\mathcal{M}_b\sigma_a &= 0 \\
P_a^+ + P_a^- &= P_b^+ + P_b^- \\
\sigma_a &= \sigma_b
\end{aligned} \tag{15}$$

Once again, in the particular case where $P_a^+ \neq 0$ and $\sigma_a = 0$, Eqs. (15) allow recovering the expression given in (9) for the acoustic response of the choked nozzle to an acoustic excitation (AA):

$$\frac{P_b^+}{P_a^+}(AA) = \frac{1+\frac{\gamma-1}{2}\mathcal{M}_2}{1+\frac{\gamma-1}{2}\mathcal{M}_1} \tag{16}$$

In the same way, if $P_a^+ = 0$ and $\sigma_a \neq 0$ are assumed, the acoustic response to an entropy perturbation (SA) is recovered as in (9), viz.:

$$\frac{P_b^+}{\sigma_a}(SA) = \frac{\mathcal{M}_2 - \mathcal{M}_1}{2}\frac{\frac{1}{2}}{1+\frac{\gamma-1}{2}\mathcal{M}_1} \tag{17}$$

Yet, for all cases where the back-pressure is below the critical pressure $p^\star$ yielding the sonic throat, a residual shock stands in the diverging section of the choked nozzle, the mean flow is no longer isentropic and the interaction of the waves with the shock must be accounted for as shown in the next section.

4.2. Waves for a shock

Even though the detailed interaction of acoustic, entropy or vorticity waves with a shock wave is a complex flow phenomenon (31; 32), the wave propagation can be fully described analytically in a simplified quasi-one-dimensional situation (10). By construction the flow immediately upstream and downstream of a normal shock is supersonic and subsonic, respectively. Four waves are ingoing in this case (Fig. 10), namely P_a^+, P_a^-, σ_a and P_b^-, while only two propagate in the outward direction, viz. P_b^+ and σ_b. The derivation of the outgoing waves as a function of the ingoing ones builds upon the classical jump relations through

a normal shock which only depend on the upstream Mach number. This latter quantity is modified by the shock motion induced by the in-going waves. This yields:

$$\begin{aligned}\left(1+\mathcal{M}_a^2+2\mathcal{M}_a^2\mathcal{M}_b\right)P_b^+ + \left(1+\mathcal{M}_a^2-2\mathcal{M}_a^2\mathcal{M}_b\right)P_b^- &= \\ \left(1+\mathcal{M}_a^2+2\mathcal{M}_a\mathcal{M}_b^2\right)P_a^+ + \left(1+\mathcal{M}_a^2-2\mathcal{M}_a\mathcal{M}_b^2\right)P_a^- & \\ \left(P_b^+ + P_b^- - P_a^+ - P_a^-\right)(\gamma-1)\frac{\left(\mathcal{M}_a^2-1\right)^2}{\left[(\gamma-1)\mathcal{M}_a^2+2\right]\mathcal{M}_a^2} &= \sigma_b - \sigma_a \qquad (18)\end{aligned}$$

Equations (18) generalize the result given in (9) to the case where P_b^- is not zero and indicate that entropy fluctuations can be generated by the interaction between an acoustic wave and a shock. In the case of a perfectly reflecting outlet, a cycle of acoustic and entropic waves can be produced, which may yield an entropic-acoustic instability as described by Foglizzo and Tagger (33) in shocked accretion flows.

4.3. Application to the DLR configuration

Having derived the general transfer functions for the different types of flows in a compact converging-diverging nozzle, the relationships mimicking the EWG experiment can be derived based on the notations of Fig. 11. As mentioned above, the present focus is on the reference test case 1 in Bake *et al.* (16) of a choked nozzle with a maximum exit Mach number of 1.32. The supercritical nozzle starts at point 1 at the nozzle inlet and finishes at point 2 in the divergent section where the normal shock takes place. The normal shock relations are defined between point 2 and 3 and finally the subcritical nozzle starts at point 3, downstream of the shock, and finishes at point 4 at the end of the divergent region. Only the entropy wave generated by the electrical device, σ_1, is taken into account at the inlet. The upstream part of the nozzle with the large settling chamber is represented in a general manner by the reflection coefficient $\mathcal{R}_1 = P_1^+/P_1^-$. The subsonic nozzle outlet is also represented in a general manner by the reflection coefficient $\mathcal{R}_4 = P_4^-/P_4^+$.

For the supercritical nozzle upstream [Eqs. (15)], the in-going and out-going acoustic waves P_2^+ and P_2^- are given by

$$
\begin{aligned}
P_2^+ &= \xi_2^+ \sigma_1 \\
P_2^- &= \xi_2^- \sigma_1
\end{aligned}
$$

with:

$$
\xi_2^+ = \frac{\left[\mathcal{M}_2 - \mathcal{M}_1 - \mathcal{R}_1(\mathcal{M}_2 + \mathcal{M}_1)\right]\frac{1}{2}}{2\left[1 + \frac{\gamma-1}{2}\mathcal{M}_1 - \mathcal{R}_1(1 - \frac{\gamma-1}{2}\mathcal{M}_1)\right]} \tag{19}
$$

$$
\xi_2^- = -\frac{\left[\mathcal{M}_2 + \mathcal{M}_1 - \mathcal{R}_1(\mathcal{M}_2 - \mathcal{M}_1)\right]\frac{1}{2}}{2\left[1 + \frac{\gamma-1}{2}\mathcal{M}_1 - \mathcal{R}_1(1 - \frac{\gamma-1}{2}\mathcal{M}_1)\right]} \tag{20}
$$

For the particular case where no reflection is considered at the inlet ($\mathcal{R}_1 = 0$) Eqs. (19) and (20) reduce to relations that can be found in (9)

$$
\begin{aligned}
\xi_2^+ &= \frac{\mathcal{M}_2 - \mathcal{M}_1}{2}\frac{\frac{1}{2}}{1 + \frac{\gamma-1}{2}\mathcal{M}_1} \\
\xi_2^- &= -\frac{\mathcal{M}_2 + \mathcal{M}_1}{2}\frac{\frac{1}{2}}{1 + \frac{\gamma-1}{2}\mathcal{M}_1}
\end{aligned}
$$

If one considers that:

$$
\begin{aligned}
\alpha_3^\pm &= 1 + \mathcal{M}_2^2 \pm 2\mathcal{M}_2^2\mathcal{M}_3 \\
\alpha_2^\pm &= 1 + \mathcal{M}_2^2 \pm 2\mathcal{M}_2\mathcal{M}_3^2
\end{aligned}
$$

and

$$
\Sigma = (\gamma - 1)\frac{\left(\mathcal{M}_2^2 - 1\right)^2}{\left[(\gamma - 1)\mathcal{M}_2^2 + 2\right]\mathcal{M}_2^2}
$$

at the normal shock [Eqs. (18)], the following relationships hold

$$
\alpha_3^+ P_3^+ + \alpha_3^- P_3^- = \alpha_2^+ P_2^+ + \alpha_2^- P_2^- \tag{21}
$$

and

$$
\left(P_3^+ + P_3^- - P_2^+ - P_2^-\right)\Sigma = \sigma_3 - \sigma_1 \tag{22}
$$

For the subcritical nozzle downstream [Eq. (10)], the in-going and out-going acoustic waves P_3^+, P_3^-, P_4^+ and P_4^- are given by

$$
\begin{aligned}
\beta_3^+ P_3^+ + \beta_3^- P_3^- &= \beta_4^+ P_4^+ + \beta_4^- P_4^- \\
\delta_3^+ P_3^+ + \delta_3^- P_3^- &= \delta_4^+ P_4^+ + \delta_4^- P_4^- + (\zeta_3 - \zeta_4)\ \sigma_3
\end{aligned} \tag{23}
$$

with

$$\beta^{\pm} = 1 \pm \frac{1}{\mathcal{M}}; \qquad \delta^{\pm} = \frac{(\gamma-1)\ (1 \pm \mathcal{M})}{1 + \frac{\gamma-1}{2}\ \mathcal{M}^2}; \qquad \zeta = \frac{1}{1 + \frac{\gamma-1}{2}\ \mathcal{M}^2}$$

Eqs. (21) and (22) combined with Eqs. (23) yield the following coupled system of equations

$$\begin{bmatrix} \alpha_3^+ & \alpha_3^- & 0 & 0 \\ \Sigma & \Sigma & -1 & 0 \\ \beta_3^+ & \beta_3^- & 0 & -\left(\beta_4^+ \mathcal{R}_4 + \beta_4^-\right) \\ \delta_3^+ & \delta_3^- & \zeta_4 - \zeta_3 & -\left(\delta_4^+ \mathcal{R}_4 + \delta_4^-\right) \end{bmatrix} \begin{bmatrix} P_3^+ \\ P_3^- \\ \sigma_3 \\ P_4^- \end{bmatrix} = \begin{bmatrix} \alpha_2^+ \xi_2^+ + \alpha_2^- \xi_2^- \\ \Sigma\left(\xi_2^+ + \xi_2^-\right) - 1 \\ 0 \\ 0 \end{bmatrix} \sigma_1 \tag{24}$$

which provide the remaining four unknowns.

4.4. Analytical results

Solving for the equations in Sec. 4.3 yields the time traces of the pressure fluctuations downstream of the throat. The acoustic waves in the duct upstream of the nozzle are assumed to propagate at the speed of sound since the Mach number is small, so that one can write $\mathcal{R}_1 = \mathcal{R}_{\text{in}} \exp(-2\imath\ell_{\text{in}}\omega/c)$, where $\mathcal{R}_{\text{in}}$ is the reflection coefficient at the duct inlet. The cross-section area of the settling chamber being large compared to the cross-section area of the duct, the pressure fluctuations are assumed to be negligible and thus one can write

$\mathcal{R}_{\text{in}} = -1$. Similarly, the reflection coefficient of the subsonic nozzle outlet can be defined with the outlet reflection coefficient of the numerical simulation as $\mathcal{R}_4 = \mathcal{R}_{\text{out}} \exp(-2\imath\ell_{\text{out}}\omega/c)$ to match the condition used in the computation. The time evolution of the entropy wave is proportional to the one imposed in the source term of the energy equation in the numerical computation. The discrete Fourier transform of this signal $\sigma_1(\omega_k)$ is used for the analytical calculations.

Calculations [solving Eq. (24)] are performed for each frequency in order to take into account the frequency-dependence of the inlet and outlet boundary conditions, but the different nozzle elements are still assumed to be compact. Since a shock is present in the divergent part of the nozzle, the supercritical section (from 1 to 2) can be treated independently of the downstream elements, and provide explicitly the waves P_2^+, P_2^- and σ_2 entering the downstream elements. The shock (from 2 to 3) and the subcritical nozzle with the outlet BC (from 3 to 4) have to be treated together since most waves are coupled to yield the full system shown in Eq. (24). Finally, the reduced pressure fluctuation $[p'/\gamma p(\omega_k)]_4$ is obtained in the frequency domain as a function of the four Mach numbers $\mathcal{M}_1$, $\mathcal{M}_2$, $\mathcal{M}_3$ and $\mathcal{M}_4$ ($\mathcal{M}_3$ and $\mathcal{M}_4$ are actually linked by the shock relations), the reflection coefficients $\mathcal{R}_{\text{in}}(\omega_k)$, $\mathcal{R}_{\text{out}}(\omega_k)$ and the reduced entropy fluctuation $\sigma_1(\omega_k)$.

The time evolutions of the pressure fluctuations reconstructed from the analytical calculations (inverse discrete Fourier transform) are compared to the numerical computations in two cases at the outlet: the non-reflecting case on the one hand (run 2D-1), and the *real* reflecting case with the set of parameters of the tuned reflection coefficient (κ and ℓ_{out}) on the other hand (run 2D-4). Figure 12 shows these comparisons when no reflection is considered at the inlet. A good agreement is found which shows that the EWG experiment (for this regime) is essentially driven by linear quasi-1-D acoustics. Yet, the levels of the analytical calculation are slightly under-predicted. When considering a more realistic impedance at the inlet, Fig. 13 shows that the levels are now well recovered for both calculations with the two different outlet boundary conditions.

Finally, the analytical method can also be used to suggest improvements to

the experimental set-up which would allow a clear separation of the indirect noise pressure signal and of acoustic reflection. An obvious solution would be to make the inlet and outlet termination fully anechoic to attenuate the reflections. This is difficult to achieve in practice, and a simpler solution is to perform the split between generated and reflected waves by either changing the duration of the temperature pulse upstream or modifying the length of the upstream and downstream ducts to increase the waves travel times. If one considers the original pulse duration T_p of 100 ms, the length of the ducts upstream and downstream of the nozzle would have to be of the order of 35 m to avoid interaction with the reflected waves before 200 ms. This is probably difficult to establish on the real experimental set-up. But, if shorter pulses are generated ($T_p = 5$ ms) and if the inlet duct length is of the order of the outlet one ($\ell_{\text{in}} = 2100$ mm), the two emitted acoustic waves (upstream and downstream) can be separated from the reflected waves if one considers only the waves travel durations. For this last case, the analytical calculations show that the duration between two pulses has to be increased until about 10 s if one wants the cycle of reflections, to be sufficiently attenuated to avoid perturbation of the theoretical pressure signal. One can see Fig. 14 the temporal evolution of the pressure fluctuation with the previous parameters. These analytical calculations were performed with and without reflections at the inlet and outlet. The pressure signal is not perturbed until the noise generation is finished ($t \approx 20$ ms) so that the true indirect noise could be investigated in the absence of interference from reflected waves.

5. Conclusions

The DLR EWG experiment of Bake *et al.* (16) has been studied numerically and analytically. Simulations have been performed both in an axisymmetric and a fully three-dimensional configuration with various duct lengths and boundary conditions accounting for acoustic reflections. In parallel, an analytical model of the full experiment, based on an extension of the theory for compact nozzles

originally derived by Marble and Candel (9), has been constructed: it takes into account the general acoustic impedances both at the inlet and outlet of the experimental set-up. The numerical and analytical analysis performed in this study demonstrate that the pressure signals obtained in the EWG experiment by Bake *et al.* (14) result from two main mechanisms: the entropy-to-acoustic conversion due the strong mean velocity gradient in the nozzle, including the normal shock that stands just downstream of the throat on the one hand; the acoustic reflection within the exhaust system downstream of the nozzle and test section on the other hand.The first mechanism is the indirect noise source and was the objective of the experiment. The second mechanism, however, is an undesired perturbation due to the non perfectly anechoic termination of the outlet, as well as the reflective inlet, which both must be understood to extract indirect noise signal from the measurements. The analysis also shows that, in the low-frequency range investigated, only 1-D planar waves are present and the compact nozzle approximation is valid, even for the entropy perturbations. As a result, the pressure signals observed experimentally and numerically can be nicely reproduced by a simple quasi-1-D analytical model derived in the low-frequency limit for the nozzle. This simpler model can also provide some guidance on how to re-design the experiment to remove or minimize the acoustic reflections in the measured pressure signals.

References

[1] G. F. Pickett, Core engine noise due to temperature fluctuations convecting through turbine blade rows, in: 2nd AIAA Aeroacoustics Conference, Vol. Paper AIAA-1975-528, 1975.

[2] N. Cumpsty, F. Marble, The interaction of entropy fluctuations with turbine blade rows ; a mechanism of turbojet engine noise, Proceedings of the Royal Society A 357 (1977) 323–344.

[3] M. Muthukrishnan, W. Strahle, D. Neale, Separation of hydrodynamic,

entropy, and combustion noise in a gas turbine combustor, AIAA Journal 16 (4) (1978) 320–327.

[4] M. Ihme, H. Pitsch, D. Bodony, Radiation of noise in turbulent non-premixed flames, Proceedings of the Combustion Institute 32 (1) (2008) 1545–1553.

[5] W. Strahle, On combustion generated noise, Journal of Fluid Mechanics 49 (2) (1971) 399–414.

[6] W. Strahle, M. Muthukrishnan, Thermocouple time constant measurement by cross power spectra, AIAA Journal 14 (11) (1976) 1642–1644.

[7] M. Bohn, Response of a subsonic nozzle to acoustic and entropy disturbances, Journal of Sound and Vibration 52 (2) (1977) 283–297.

[8] W. Strahle, Combustion noise, Progress in Energy and Combustion Science 4 (3) (1978) 157–176.

[9] F. Marble, S. Candel, Acoustic disturbances from gas nonuniformities convected through a nozzle, Journal of Sound and Vibration 55 (1977) 225–243.

[10] W. Moase, M. Brear, C. Manzie, The forced response of choked nozzles and supersonic diffusers, Journal of Fluid Mechanics 585 (2007) 281–304.

[11] S. R. Stow, A. P. Dowling, T. P. Hynes, Reflection of circumferential modes in a choked nozzle, Journal of Fluid Mechanics 467 (2002) 215–239.

[12] F. Bake, U. Michel, I. Rohle, C. Richter, F. Thiele, M. Liu, B. Noll., Indirect combustion noise generation in gas turbines, in: 11^{th} AIAA/CEAS Aeroacoustics Conference, Vol. Paper AIAA-2005-2830, Monterey, CA, 2005.

[13] F. Bake, U. Michel, I. Röhle, Investigation of entropy noise in aero-engine combustors, Journal of Engineering for Gas Turbines and Power 129 (2) (2007) 370–376.
URL `http://elib.dlr.de/49128`

[14] F. Bake, N. Kings, I. Röhle, Fundamental mechanism of entropy noise in aero-engines: Experimental investigation, Journal of Engineering for Gas Turbines and Power 130 (1) (2008) 011202–1 – 011202–6.
URL http://elib.dlr.de/57707

[15] F. Bake, N. Kings, A. Fischer, I. Rohle, Experimental investigation of the entropy noise mechanism in experimental investigation of the experimental investigation of the entropy noise mechanism in aero-engines, International Journal of Aeroacoustics 8 (1) (2009) 125–142.

[16] F. Bake, C. Richter, B. Mühlbauer, N. Kings, I. Röhle, F. Thiele, B. Noll, The entropy wave generator (ewg): a reference case on entropy noise, Journal of Sound and Vibration 326 (2009) 574–598.

[17] B. Mühlbauer, B. Noll, M. Aigner, Numerical investigation of entropy noise and its acoustic sources in aero-engines, in: ASME Turbo Expo 2008, Vol. GT2008-50321, Berlin, Germany, 2008.

[18] M. Leyko, F. Nicoud, T. Poinsot, Comparison of direct and indirect combustion noise mechanisms in a model combustor, AIAA Journal In press.

[19] P. Schmitt, T. Poinsot, B. Schuermans, K. P. Geigle, Large-eddy simulation and experimental study of heat transfer, nitric oxide emissions and combustion instability in a swirled turbulent high-pressure burner, Journal of Fluid Mechanics 570 (2007) 17–46.

[20] T. Poinsot, D. Veynante, Theoretical and Numerical Combustion, R.T. Edwards, 2nd edition, 2005.

[21] O. Colin, M. Rudgyard, Development of high-order Taylor-Galerkin schemes for unsteady calculations, Journal of Computational Physics 162 (2) (2000) 338–371.

[22] B. Mühlbauer, B. Noll, M. Aigner, Numerical investigation of the fundamental mechanism for entropy noise generation in aero-engines, Acta Acustica united with Acustica 95 (2009) 470–478.

[23] M. Leyko, F. Nicoud, S. Moreau, T. Poinsot, Numerical and analytical investigation of the indirect noise in a nozzle, in: Proceedings of the Summer Program, Center for Turbulence Research, NASA AMES, Stanford University, USA, 2008, pp. 343–354.

[24] M. Leyko, F. Nicoud, S. Moreau, T. Poinsot, Numerical and analytical investigation of the indirect combustion noise in a nozzle, Comptes Rendus Mécanique 337 (2009) 415–425.

[25] Y. Reymen, M. Baelmans, D. W., Efficient implementation of tam and auriault's time-domain impedance boundary condition, AIAA Journal 46 (9) (2008) 2368–2376.

[26] C. Tam, L. Auriault, Time-domain impedance boundary conditions for computational aeroacoustics, AIAA Journal 34 (5) (1996) 917–923.

[27] S. Rienstra, Impedance models in time domain including the extended helmholtz resonator model, in: 12^{th} AIAA/CEAS Aeroacoustics Conference, Vol. Paper AIAA-2006-2686, Cambridge, MA, 2006.

[28] Y. Ozyoruk, L. Long, M. G. Jones, Time-domain numerical simulation of a flow-impedance tube, Journal of Computational Physics 146 (1998) 29–57.

[29] T. Poinsot, S. Lele, Boundary conditions for direct simulations of compressible viscous flows, Journal of Computational Physics 101 (1) (1992) 104–129.

[30] L. Selle, F. Nicoud, T. Poinsot, The actual impedance of non-reflecting boundary conditions: implications for the computation of resonators, AIAA Journal 42 (5) (2004) 958–964.

[31] K. Mahesh, S. Lee, S. Lele, P. Moin, The interaction of an isotropic field of acoustic waves with a shock wave, Journal of Fluid Mechanics 300 (1995) 383–407.

[32] K. Mahesh, S. Lele, P. Moin, The influence of entropy fluctuations on the interaction of turbulence with a shock, Journal of Fluid Mechanics 334 (1997) 353–379.

[33] T. Foglizzo, M. Tagger, Entropic-acoustic instability in shocked accretion flows, Astrnomy and Astrophysics 363 (2000) 174–183.

List of Figures

List of Tables

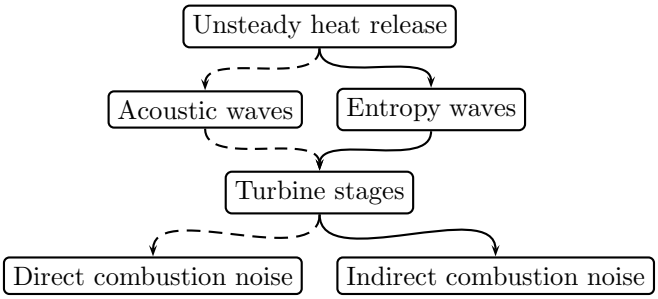

Figure 1: The two main mechanisms for noise generation from confined flames: direct (- - - -) and indirect (———) noise.

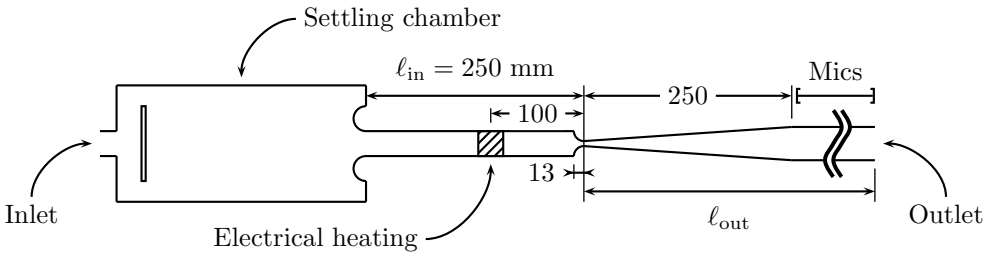

Figure 2: Sketch of the Entropy Wave Generator experimental set-up (lengths are given in mm). Short configuration: $\ell_{\text{out}} = 500$ mm; Long configuration: $\ell_{\text{out}} = 2100$ mm

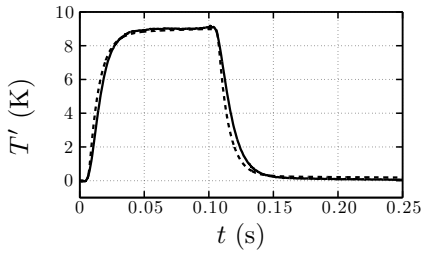

Figure 3: Time traces of the experimental (———) and numerical (- - - -) temperature downstream of the heating location.

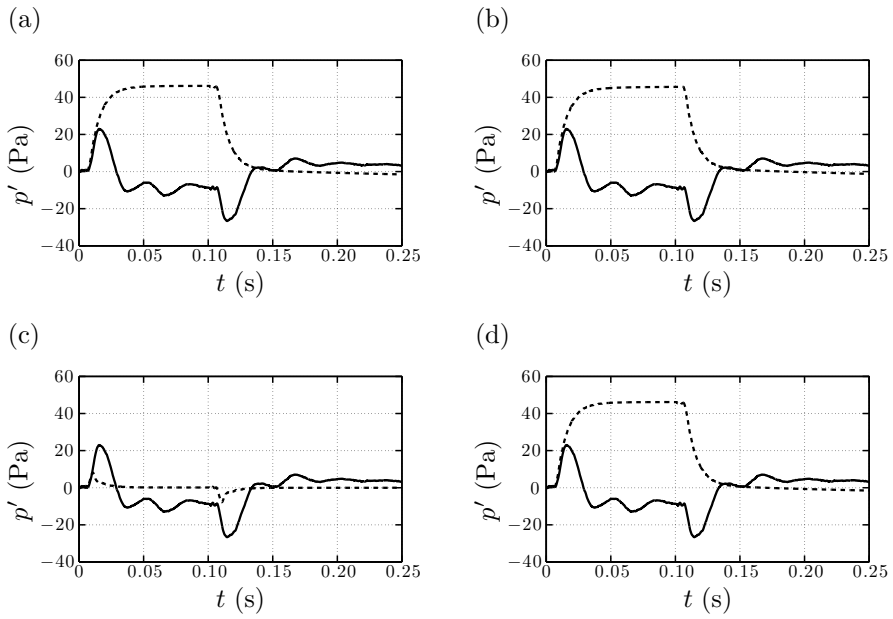

Figure 4: Time traces of the fluctuating pressure 350 mm downstream of the nozzle. Experimental data: ——— ; Numerical result: - - - - . (a) Run 2D-1; (b) Run 2D-2; (c) Run 2D-3; (d) Run 3D-1.

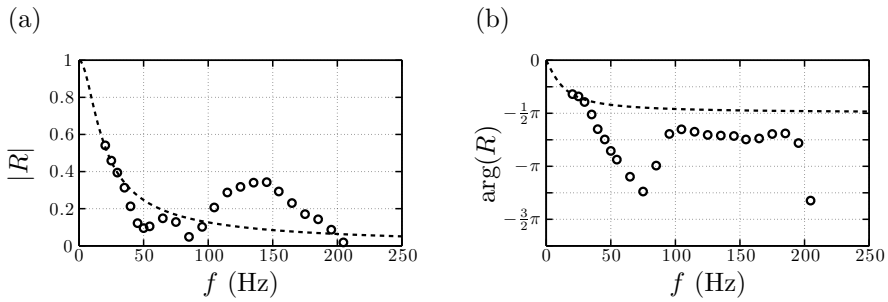

Figure 5: Experimental reflection coefficient shifted 2100 mm downstream of the nozzle throat and numerical reflection coefficient. Shifted experimental data: ∘ ; Tuned relaxation coefficient: – – – – . (a) Modulus; (b) Argument.

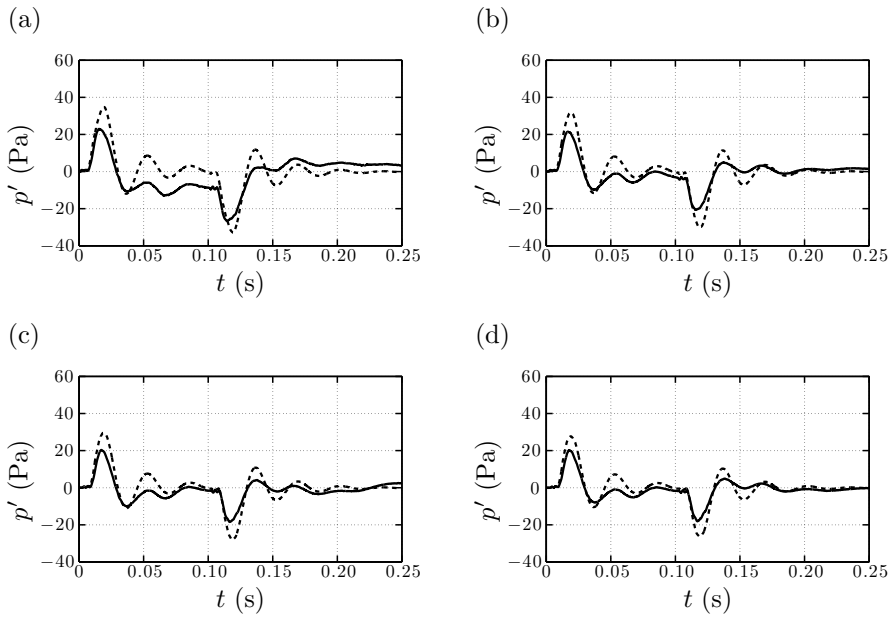

Figure 6: Time traces of the fluctuating pressure downstream of the nozzle. Experimental data: ——— ; Run 2D-4: – – – – . Distance downstream of the nozzle: (a) 350 mm; (b) 730 mm; (c) 975 mm; (d) 1150 mm.

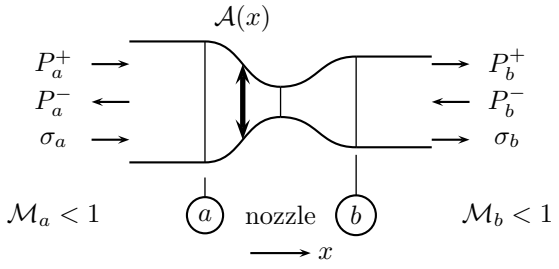

Figure 7: Sketch of the unchoked nozzle case.

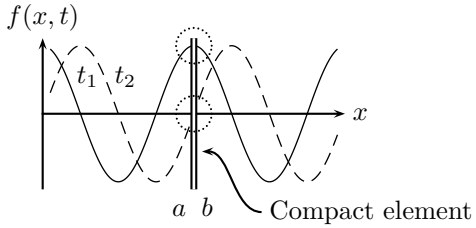

Figure 8: Compact element illustration: The quantity f, conserved throughout the element, is the same upstream (a) and downstream (b) at each instant.

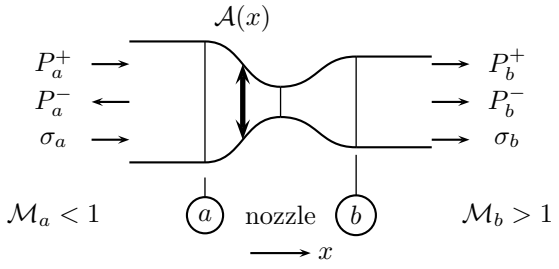

Figure 9: Sketch of the isentropic choked nozzle case.

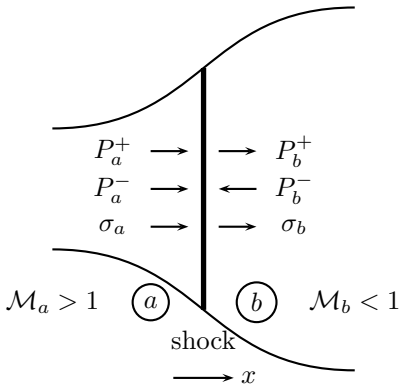

Figure 10: Sketch of the supersonic flow with normal shock case.

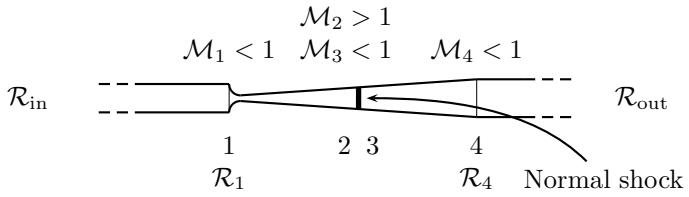

Figure 11: Description of the analytic approach

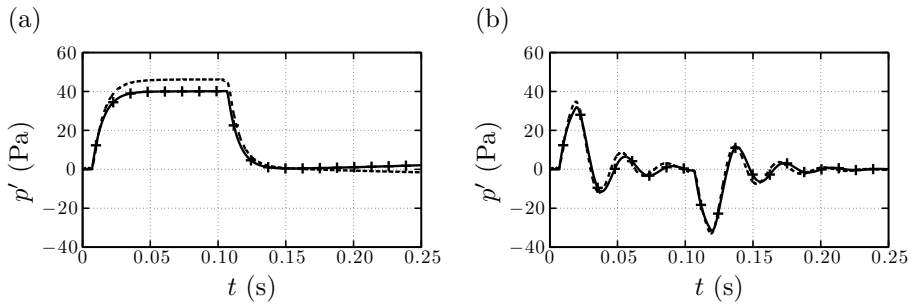

Figure 12: Time traces of the fluctuating pressure downstream of the nozzle. Numerical results: – – – – ; Analytical results without reflections at the inlet and $\ell_{\text{out}} = 2100$ mm: $-+-$. (a) Non-reflecting case (Analytic compared to Run 2D-1); (b) Finite impedance case (Analytic compared to Run 2D-4).

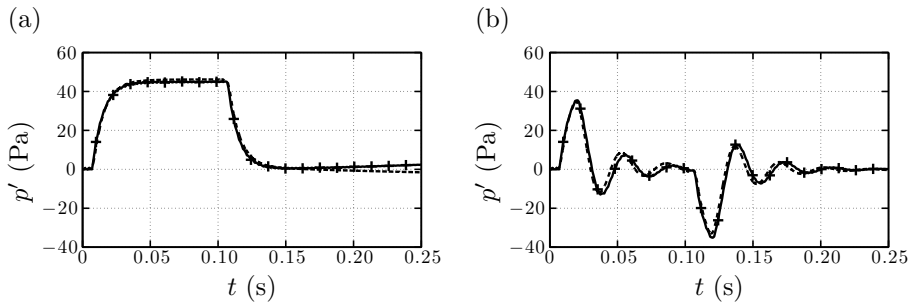

Figure 13: Time traces of the fluctuating pressure downstream of the nozzle. Numerical results: - - - - ; Analytical results with reflections at the inlet and $\ell_{\text{out}} = 2100$ mm: $- + -$. (a) Non-reflecting case (Analytic compared to Run 2D-1); (b) Finite impedance case (Analytic compared to Run 2D-4).

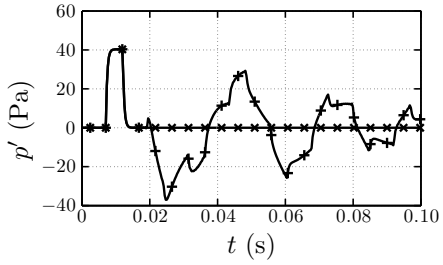

Figure 14: Analytical time traces of the fluctuating pressure downstream of the nozzle with shorter pulse duration. Totally non-reflecting at inlet and outlet: $- \times -$; Reflections at inlet and outlet: $- + -$.